Conceptual investigation of a novel air-cooled window for a recuperated solar-dish Brayton cycle using a turbocharger and short-term thermal storage

Henno de Beer
Supervisor: Prof Willem le Roux, Co-supervisor: Prof Josua Meyer
University of Pretoria, Department of Mechanical and Aeronautical Engineering
Email: henno.debeer@gmail.com

Centre for Renewable and Sustainable Energy Studies

Abstract
A recuperated solar-dish Brayton cycle using an off-the-shelf turbocharger as a micro-turbine and a rectangular cavity receiver with integrated thermal storage was considered for this study. These solar receivers have a considerable amount of heat loss to the environment. It was proposed to have a glass channel parallel to each of the four receiver walls on the inside of the cavity receiver. The glass channel is made up of two glass walls and is to be cooled by air flowing from the compressor. This conceptual study used an entropy generation minimisation technique combined with a SolTrace analysis to investigate the impact of the air-cooled window on the performance of the cycle. Results showed that the maximum solar-to-mechanical efficiencies were between 44% and 47% lower than for the cycle without the window. The exhaust temperature of the cycle with the window was higher than that of the cycle without the window, which led to a higher energy utilisation factor of between 7% and 18% if the exhaust was used for cogeneration. Therefore, this conceptual study indicated that it might not be feasible to implement the cooling window, except where a higher cycle exhaust temperature was preferred for cogeneration.

Keywords: Solar-dish, micro-turbine, cooling window, recuperator, Brayton cycle.

1 Introduction
In this research, a novel air-cooled glass window was proposed to be placed on the inside of the receiver cavity, parallel to the receiver walls and perpendicular to the aperture in an effort to minimise the heat losses from the receiver. A recuperated solar dish Brayton cycle using an off-the-shelf turbocharger as a micro-turbine and open-cavity tubular receiver with integrated phase-change material was considered.

1.1 Background
Heat losses from an open-cavity solar receiver can negatively impact the thermal and solar-to-mechanical efficiency of the system. The thermal losses of an open-cavity solar receiver include the convective and radiative losses from the cavity to the surroundings as well as the conductive heat losses through the insulation. Craig et al. (2020) conducted a study based on a similar receiver considered in the work of Le Roux and Sciacovelli (2019). By using ray tracing and CFD, Craig et al. (2020) found that the receiver had a total heat loss rate of 6.8 kW relative to a rated solar input power of 12.7 kW at a 0° inclination angle and an average receiver inner-surface temperature of 780 °C. Le Roux and Sciacovelli (2019) also found that the maximum total heat loss rate from the solar receiver was in the range of 12 kW for a receiver with a PCM at 1200 K and an inclination angle of 45°. Heat losses from the solar receiver can be decreased by decreasing the size of the aperture; however, this leads to the need for a more accurate and more expensive solar dish. Some research used glass covers in order to minimise heat losses from rectangular solar receivers (Cui et al., 2013, Fischer & Hahne, 2000, Fuqiang et al., 2014, Subedi et al., 2019). However, keeping the glass covers cool under highly concentrated solar irradiation has proven to be a difficult task. A window

cover on a solar receiver that is not cooled can crack or shatter due to the very high temperatures the glass is subjected to. This can lead to cost increases for the system as well as pose safety hazards to the operators or maintenance personnel of the system.

1.2 System description

A glass window was proposed on the inside of the receiver cavity, parallel to the rectangular receiver walls. This concept consisted of two glass panes forming a channel, in which cooling air flows (see Figure 1b). There were four channels, one on each side of the receiver, as well as a channel parallel to the top wall of the receiver. The glass was cooled by air coming directly from the compressor. Figure 1a shows the recuperated solar dish Brayton cycle with short-term thermal storage as well as the position of the novel cooling window (in blue), which was the focus of investigation in this work. The cycle used air as a working fluid in an open-cycle configuration.

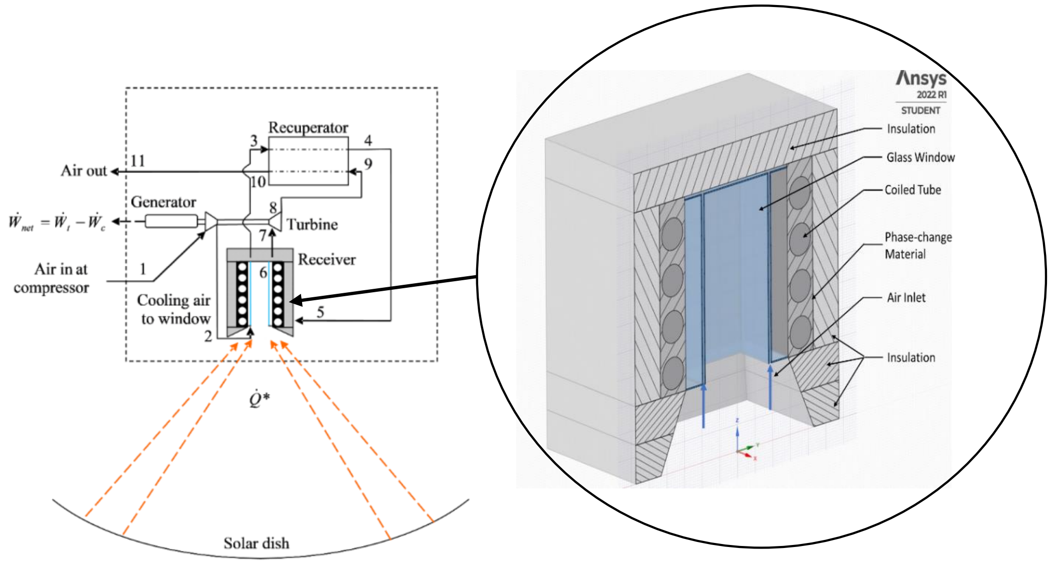

a) Solar dish Brayton cycle b) 3D section view of receiver

Figure 1. a) Recuperated solar dish Brayton cycle with receiver window cooling, adapted from Le Roux and Sciacovelli (2019). b) 3D section view of the receiver with the cooling window concept.

1.3 Objectives

The research objectives included analysing the impact of the cooling window on the solar-to-mechanical efficiency and energy utilisation factor using numerical methods. The glass surface temperature was another important property by which the impact of the cooling window would be measured. A comparison between the different performance parameters for this novel cooling window and the solar receiver without the cooling window would be made. The results of this study will be compared to work of Le Roux and Sciacovelli (2019). This comparison should provide a clear understanding of the impact of the cooling window on the performance of the solar-dish Brayton cycle. Essentially, the conceptual study investigated whether the cooling window was feasible to reduce the heat losses of the solar receiver, while maintaining acceptable solar-to-mechanical efficiencies.

2 Research methodology

2.1 Assumptions

The dish surface was modelled as having a reflectivity of 85%, a rim angle of 45° and both a specularity and slope error of 2 mrad. The receiver cavity walls were modelled as oxidised stainless steel with an assumed reflectance of 15% (Le Roux et al., 2014). The emissivity of the inner-cavity wall was assumed to be 0.7 for oxidised stainless steel at 1000 K (Le Roux & Sciacovelli, 2019). It was assumed that the phase-change material, as well as the stainless steel inner-cavity walls and the tube surface, was at a constant temperature (the melting temperature of the PCM). It was assumed that the mass flow rate from the compressor was divided equally between the five window channels and that each glass window was 3 mm thick. The glass had an assumed reflectivity of 8%, transmissivity of 86% and absorptivity of 6% for solar radiation per window (Çengel & Ghajar, 2015). Since there were two glass panes per channel, the effective transmissivity for infrared radiation from the inner-cavity walls became almost negligible. Therefore, in this work, it was assumed that for infrared radiation, the reflectivity and absorptivity of the double-glass window were 90% and 10% respectively. The emissivity of the glass was assumed to be constant at 0.88 (Subedi et al., 2019). The radiation heat transfer from a hot surface to a cooler surface is proportional to the fourth power of the surface temperature of the two surfaces. To be able to use Gaussian elimination, the fourth-power temperature terms were assumed to have a linear form, $m_1 T_{s,n} + c_1$, according to Le Roux et al. (2014). For radiation heat loss from the glass between 500 K and 800 K, a linear regression line with a coefficient of determination of 0.96 was used. Conduction heat losses from the cooling window were not considered in this study and were expected to be negligible. The width between the two glass panes forming the channel was initially arbitrarily chosen as 6.8 mm and the simulations were carried out with this channel width; however, the channel width was also investigated as a parameter.

2.2 Receiver glass modelling

Each of the four sides of the cooling channels was divided into sections (as will be discussed in section 2.2.5) and the temperature and heat flux on each of the sections were calculated by using a similar methodology to the one used by Le Roux et al. (2014) to calculate the temperature of the coiled tube in the receiver. The receiver and the glass window were modelled using the first law of thermodynamics.

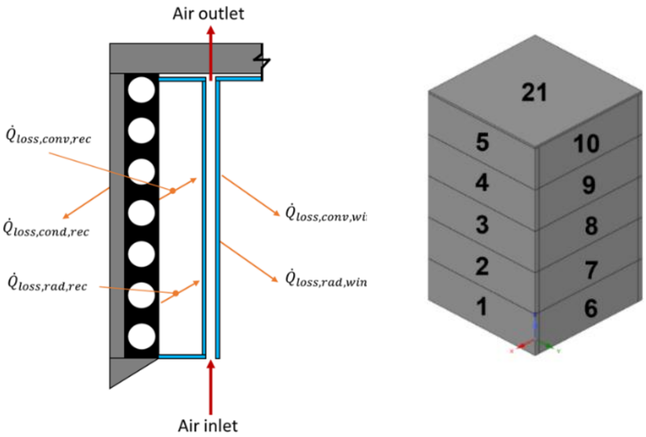

a) b)

Figure 2. a) 2D section view of the receiver with heat losses. b) Numbering system used for glass sections.

Figure 2a shows the heat losses from the window to the environment through the receiver aperture as well as the heat gain on the window from the inner-receiver wall. The net heat transfer rate at the glass window is given by:

$$\dot{Q}_{net,win} = \dot{Q}^*_{win} + \dot{Q}_{abs} - \dot{Q}_{loss,rad,win} - \dot{Q}_{loss,conv,win} \quad (1)$$

where $\dot{Q}_{abs} = \dot{Q}_{loss,rad,rec} + \dot{Q}_{loss,conv,rec}$, which represents the rate of heat gain on the window from the inner-receiver wall (see Figure 2a), while $\dot{Q}^*_{win}$ represents the absorbed solar heat transfer rate as found from SolTrace (see the following subsection for a description of the SolTrace analysis).

2.2.1 SolTrace model

SolTrace can model concentrated solar power (CSP) systems using Monte Carlo ray-tracing methodologies (Wendelin et al., 2013). SolTrace has a fast and powerful script engine that allows the user to automate the analysis and run multiple different geometries, sun definitions or optical properties (Wendelin et al., 2013). The script was written in such a way that when the dish size was changed, the receiver position relative to the solar dish would be adjusted accordingly to have the parabolic dish's focal point on the receiver with minimal spillage. A pillbox sunshape was assumed with the parameter for the pillbox chosen as the half-angle width of 4.65 mrad. Each of the glass panes was modelled with a refraction index of 1.5, with an air entity on each side with a refraction index of 1. This was done to capture the refraction of light as it travelled through the glass, as recommended by Wendelin et al. (2013). A million sunrays were used with a seed value of '123' throughout the SolTrace simulations.

2.2.2 Radiation heat loss model

The radiation heat loss rate from a surface can typically be calculated with Eq. (2):

$$\dot{Q}_{loss,rad} = \varepsilon\sigma A(T_s^4 - T_\infty^4) \tag{2}$$

When calculating the surface temperature of the glass, the view factor (sometimes called the shape factor) is a very important aspect to consider. The view factor determines how much a certain part of the glass is exposed to the aperture (environment), inner-cavity wall, or the other glass panes. The radiation heat transfer rate in different sections of the inner-receiver wall was calculated by using Eq. (3) (Le Roux et al., 2014):

$$\dot{Q}_{loss,rad,n} = A_n \sum_{j=1}^{N} F_{n\rightarrow j}\left(\varepsilon_n \sigma T_{s,n}^4 - \varepsilon_j \sigma T_{s,j}^4\right) \tag{3}$$

The radiation heat loss rate from the receiver depended on the emissivity of the receiver wall. Eq. (3) was also used to determine the radiation heat loss rate from the glass to the aperture.

2.2.3 Convection heat loss model

Convection heat transfer will occur on the inside of the cavity, on the inside of the cooling channel, on the inside of the air gap between the window and the cavity wall, and on the inside of the coiled tubes in the receiver. The same forced convection model on the inside of the coiled tubes was used as the one in the work of Le Roux and Sciacovelli (2019). The natural convection model from Paitoonsurikarn and Lovegrove (2006) was used and their results showed small differences between their newly developed correlation and numerical simulations. Their Nusselt number correlation, based on the Rayleigh and Prandtl numbers for receivers, was derived through free convection heat loss simulations. Paitoonsurikarn and Lovegrove (2006) showed that a parameter described as the ensemble cavity length scale, L_s, could be used to account for the effects of cavity geometric parameters and inclination angle (Paitoonsurikarn & Lovegrove, 2003, Paitoonsurikarn et al., 2004). This proposed ensemble length, L_s, is given by Eq. (4) (Paitoonsurikarn & Lovegrove, 2006):

$$L_s = \left|\sum_{i=1}^{3} a_i \cos(\phi + \psi_i)^{b_i} L_i\right| \tag{4}$$

Eq. (4) depends on the cavity dimensions as well as the inclination angle (ϕ) of the receiver. The index, *i*, in Eq. (4), depends on three length scales of the receiver, namely the width, depth and aperture size, which is represented by the symbol L_i in Eq. (4). The constants a_i, b_i and ψ_i from Eq. (4) are summarised in Table 1. Paitoonsurikarn and Lovegrove (2003) found the constants in Table 1 by fitting a curve to their CFD simulation results.

Table 1. Constants used in Eq. (4) from Paitoonsurikarn and Lovegrove (2006).

$\boldsymbol{i}$	$\boldsymbol{a_i}$ $(-)$	$\boldsymbol{b_i}$ $(-)$	$\boldsymbol{\psi_i}$ $(-)$
1	4.08	5.41	-0.11
2	-1.17	7.17	-0.30
3	0.07	1.99	-0.08

The modified Nusselt correlation had the following form (Paitoonsurikarn & Lovegrove, 2006):

$$Nu_L = 0.0196\, Ra_L^{0.41}\, Pr^{0.13} \tag{5}$$

The Rayleigh and Prandtl numbers in Eq. (5) were evaluated at the film temperature, which for this study, was taken to be the average between the glass surface temperature, T_s, and the ambient temperature, T_∞. The heat transfer coefficient on the inside of the cavity was then calculated by rearranging Eq. (6), with the characteristic length being the ensemble length L_s from Eq. (4).

$$Nu = \frac{hL_c}{k} \tag{6}$$

The heat loss rate due to convection per window section was then calculated with the average heat transfer coefficient for the whole cavity and is given by Eq. (7):

$$\dot{Q}_{loss,conv} = h_{cav} A_{gl} (T_s - T_\infty) \tag{7}$$

Forced internal convection occurred on the inside of the coiled tube in the receiver, on the inside of the recuperator channels and on the inside of the channel formed by two glass panes (see Figure 2a). For the coiled tube, Le Roux and Sciacovelli (2019) used the Dittus-Boelter equation, as introduced by McAdams (1942), to determine the Nusselt number and convection heat transfer coefficient. Since the glass channels and recuperator channels were rectangular, the Reynolds and Nusselt number calculations had to be altered by using the hydraulic diameter (Çengel & Ghajar, 2015).

For laminar flow, the Nusselt numbers and friction factors for the glass channels and recuperator channels are a function of the ratio of the width and the height of the rectangular channel, assuming constant heat flux (Çengel & Ghajar, 2015). The heat transfer coefficient was calculated by rearranging Eq. (6) and using the hydraulic diameter as the characteristic length.

For turbulent flow (Reynolds number greater than 4000), the Nusselt number for the glass channels and the recuperator channels are given by Eq. (8) (Gnielinski, 1976):

$$Nu = \frac{(f/8)(Re - 1000)Pr}{1 + 12.7\left(\frac{f}{8}\right)^{0.5}\left(Pr^{\frac{2}{3}} - 1\right)} \tag{8}$$

Note that the friction factor, f, in Eq. (8) was derived from the Petukhov equation (Petukhov, 1970) for turbulent flow in smooth tubes, as shown in Eq. (9):

$$f = (0.790 \ln(Re) - 1.64)^{-2} \tag{9}$$

The convection heat transfer in the enclosure (between each inner-cavity wall and glass pane, see Figure 2a) depends on the aspect ratio (AR) and Rayleigh number of the enclosure. In CFD simulations by Pendyala et al. (2015), the authors developed Nusselt number correlations applicable to air as a working fluid:

$$Nu = 1.46 \times 10^{-5} (AR)^{0.19} (\ln(Ra))^{3.228} \tag{10}$$

Eq. (10) and Eq. (6) were used to find the heat transfer coefficient in the enclosure. The convection heat loss from the window is included in Eq. (1).

2.2.4 Pressure drop

For fully developed flow in a circular duct, the pressure drop is influenced by friction, length of the duct, density and velocity and is given by Eq. (11) (Çengel & Ghajar, 2015). The only difference for a rectangular duct is that the hydraulic diameter, D_h, was used instead of the diameter, D.

$$\Delta P = f \frac{L}{D} \frac{\rho V_{avg}^2}{2} \tag{11}$$

For laminar flow in a duct with constant heat flux, the friction factor can be interpolated at the specific ratio of the channel with and height (Çengel & Ghajar, 2015). For turbulent flow, Eq. (9) can be used to calculate the friction factor in the rectangular duct. The friction factor can then be used with Eq. (11) to calculate the pressure drop in the duct.

2.2.5 Numerical methods

The temperature profile of the glass was determined by dividing each of the four glass panes into several equally sized sections (see Figure 2b). Each of the four sides of the rectangular receiver was divided into five sections, which gave each section a height of 0.1 m, with a receiver height of 0.5 m. The top section was also covered with glass in the simulation to account for the view factor to the top. The top glass pane was not divided into sections to limit computational time. Figure 2b shows the numbering system used for the glass sections, where the top section was added to the end of the numbering system. The proposed method was based on the method put forward by Le Roux et al. (2014), the main difference was that the flow was not modelled to flow in a coil but rather from the bottom to the top of the window.

The temperature profile and the net heat transfer rate at the various sections of each glass window were found with Eq. (12). It must be noted that the mass flow rate, $\dot{m}_{chn}$, used in all the equations that involved the windows was equal to the mass flow rate at Point 1 in Figure 1 divided by five.

$$\dot{Q}_{net,n,win} = \frac{\left(T_{s,n} - \sum_{i=1}^{n-1}\left(\frac{\dot{Q}_{net,i}}{\dot{m}_{chn}c_{p0}}\right) - T_{in,0}\right)}{\left(\frac{1}{h_{chn}A_n} + \frac{1}{2\dot{m}_{chn}c_{p0}}\right)} \tag{12}$$

Eq. (12) was derived from the definition of fluid temperature at the centre of a control volume as well as the definition of convection heat transfer, according to Eq. (13) and Eq. (14) respectively.

$$T_{f,n} = T_{in,n} + \frac{T_{out,n} - T_{in,n}}{2} = T_{in,n} + \frac{\dot{Q}_{net,n,win}}{2\dot{m}_{chn}c_{p0}} \tag{13}$$

$$\dot{Q}_{net,n,win} = h_{chn}A_n\left(T_{s,n} - T_{f,n}\right) \tag{14}$$

Eq. (12) used the outlet temperature of the compressor as $T_{in,0}$. The outlet air temperature from each section, $T_{out,n}$, was calculated from the heat gained at the previous glass sections. Eq. (6) and Eq. (8) was used to calculate the heat transfer coefficient in Eq. (12). By using Eq. (3) and Eq. (7) and substituting into Eq. (1), Eq. (15) could be found, which was written in terms of the unknown net heat transfer rates and surface temperatures of each glass section according to the numbering in Figure 2. Note that for the radiation heat loss term, the radiation heat transfer from one glass side to another and the radiation heat loss to the aperture were included. This equation could be simplified further by using the linear approximation (as discussed in Section 2.1).

$$\begin{aligned}\dot{Q}_{net,n,win} = \dot{Q}^*_{n,win} + \dot{Q}_{abs,n} - A_n\varepsilon\sigma\left(m_1T_{s,n} + c_1\right) + A_n\varepsilon\sigma\sum_{j=1}^{N}F_{n\to j}\left(m_1T_{s,j} + c_1\right)\\ + A_n\varepsilon_\infty\sigma F_{n\to\infty}T_\infty^4 - h_{n,cav}A_n\left(T_{s,n} - T_\infty\right)\end{aligned} \tag{15}$$

The $\dot{Q}_{abs,n}$ term in Eq. (15) is the radiation and convection heat transfer that was transferred from the inner-receiver wall to the window. Eq. (5) was used to calculate the heat transfer coefficient in Eq. (15). By using Gaussian elimination in *Octave*, the surface temperatures ($T_{s,n}$) and net heat transfer rates ($\dot{Q}_{net,n,win}$) of the window could be calculated by solving Eq. (12) and Eq. (15) simultaneously. The outlet air temperature of the cooling window was also of importance because the outlet air was directly fed back into the Brayton cycle (Position 3 in Figure 1). The outlet air temperature was calculated by rearranging Eq. (16) and solving for $T_{a,out}$.

$$\dot{Q}_{net,win} = \dot{m}_{chn}c_p\left(T_{a,out} - T_{a,in}\right) \tag{16}$$

The mass flow rate in Eq. (16) was calculated based on the corrected mass flow rate of each turbocharger. Eq. (16) could also be used to check whether the Gaussian elimination function had been solved correctly because $\dot{Q}_{net,win}$ had to be equal to the sum of the heat transfer rates that were calculated at each section of the window using Eq. (14). The outlet air temperature was used in modelling the complete cycle in the following sections.

2.3 Complete cycle modelling

The receiver phase-change temperature, chosen turbocharger, turbocharger operating point, and the cooling channel width were parameters in the study. The variables were the recuperator channel width, height, length and number of parallel flow channels, the same as those used by Le Roux and Sciacovelli (2019). The dimensions of the open-cavity tubular solar receiver stayed constant in the analysis and were the same as those used in the study by Le Roux and Sciacovelli (2019). The complete cycle was modelled in the same manner as was done in the study by Le Roux and Sciacovelli (2019), with only the modifications to equations included here.

2.3.1 Solar receiver

The aperture area of the receiver was fixed at 0.25 m × 0.25 m and the tube inner diameter was 0.0833 m. The coiled tube receiver was modelled as a constant surface temperature tube, with the assumption that the tube surface temperature, $T_{s,rec}$, was equal to the PCM melting temperature (Le Roux & Sciacovelli, 2019). For steady-state operation, the exit temperature of the receiver air was calculated with Eq. (17) and the net heat transfer rate by Eq. (18).

$$T_e = T_{s,rec} - \left(T_{s,rec} - T_i\right)e^{-\frac{h_{rec}A_s}{\dot{m}c_p}} \quad (17)$$

$$\dot{Q}_{net,rec} = h_{rec}A_s \frac{(T_i - T_e)}{\ln\left[\frac{T_{s,rec} - T_e}{T_{s,rec} - T_i}\right]} \quad (18)$$

It must be noted that the heat transfer coefficient, h_{rec}, in Eq. (18) was on the inside of the coiled tube. The required solar power at the cavity walls was found using Eq. (19).

$$\dot{Q}^*_{rec} = \dot{Q}_{loss,cond,rec} + \dot{Q}_{loss,conv,rec} + \dot{Q}_{loss,rad,rec} + \dot{Q}_{net,rec} \quad (19)$$

The heat losses due to conduction from the receiver to the environment were calculated according to Le Roux et al. (2014):

$$\dot{Q}_{loss,cond,rec} = \frac{A_c\left(T_{s,rec} - T_\infty\right)}{1.86} \quad (20)$$

where it was found that $(1/h_{outer} + t_{ins}/k_{ins}) \approx 1.86$ for receiver aperture sizes of up to 2 m (Le Roux et al., 2014). The convection heat loss from the receiver to the window through the air gap between the window was calculated with Eq. (7), where the heat transfer coefficient was calculated with Eq. (5) and the heat transfer was from the hot inner-cavity wall to the window. The radiation heat loss was calculated with a modified form of Eq. (2). Instead of having radiation heat loss to the environment, the radiation heat loss was from the inner-cavity wall to the glass, thus T_∞ in Eq. (2) was replaced by $T_{s,win}$.

The cycle optimisation code used a while loop to iterate the code and within the loop, Eq. (18) was used to calculate $\dot{Q}_{net,rec}$. The SolTrace model was run with five different solar dish sizes, namely dish diameters of 4.8, 6, 7.2, 8.4 and 9.6 m. From the SolTrace analysis, a linear relationship was found between the solar flux on the glass panes and the inner-receiver walls, i.e. the relationship between $\dot{Q}^*_{win}$ and $\dot{Q}^*_{rec}$. It is important to note that $\dot{Q}^*_{win}$ only included the solar heat flux contribution and not the reradiation from the inner-cavity wall since SolTrace could only simulate the solar heat input. The total required solar power is a summation of $\dot{Q}^*_{win}$ and $\dot{Q}^*_{rec}$ and was used further in the analysis.

The code that calculated the temperature profile of the window required the solar flux on the window to be a distribution (per window section) instead of a total that SolTrace provides. From the five SolTrace cases, the ratio of the solar flux distribution on each glass division could be found. This ratio was calculated as:

$$\Gamma = \frac{Heat\ flux\ per\ division}{Total\ heat\ flux\ per\ side} \quad (21)$$

A function was made that interpolated between the five different dish size heat flux ratios. This distribution was used as an input to the code, as discussed in Section 2.2.1. The code calculated the glass surface temperature, which was used to calculate the heat losses from the window by using Eq. (3) and Eq. (7). Eq. (19) was then used to find $\dot{Q}^*_{rec}$, which was then used in the linear relationship between $\dot{Q}^*_{win}$ and $\dot{Q}^*_{rec}$ to find $\dot{Q}^*_{win}$. The solar heat flux, $\dot{Q}^*_{win}$, was then used in Eq. (1) to find the net heat transfer rate on the window, $\dot{Q}_{net,win}$. The neat heat transfer rate was then used to find the change in temperature between Positions 2 and 3 (in Figure 1) in the cycle with:

$$\Delta T_{2-3} = \frac{\dot{Q}_{net,win}}{\dot{m}c_p} \tag{22}$$

The temperature change (Eq. (22)) was then used to calculate the temperature at Position 3 in Figure 1 as follows:

$$T_3 = T_2 + \Delta T_{2-3} \tag{23}$$

which was iterated each time the while loop was executed.

The same plate-type recuperator was considered in this study as the one studied by Le Roux and Sciacovelli (2019). The turbine pressure ratio was used as a parameter in the analysis, as was done in the work by Le Roux and Sciacovelli (2019). A turbine map was used where the pressure ratio was given as a function of the corrected mass flow rate (Le Roux & Sciacovelli, 2019).

2.3.2 Power output

Octave was to used calculate the maximum solar-to-mechanical efficiency, the net power output and the required solar input power for receiver phase-change temperatures ranging from 900 K to 1200 K while considering an off-the-shelf turbocharger and several different recuperator geometries (see Le Roux and Sciacovelli (2019)). The range of the recuperator length was changed to 0.5 to 3.5 m instead of the 1.5 to 3.5 m used in Le Roux and Sciacovelli (2019). A smaller recuperator length was expected because the air entering the recuperator at State 3 should already have gained significant heat from the window and the recuperator thus needed to exchange less heat to get the receiver inlet air to the same temperature.

The turbine map provides the corrected turbine mass flow rate in terms of the turbine pressure ratio. The actual turbine mass flow rate is a function of the turbine inlet temperature and pressure and was calculated via iteration (Le Roux & Sciacovelli, 2019). A commercial turbocharger was considered in this analysis: the *GT2052* from *Garret Motion* in the USA. The *Octave* program had the same structure as described in Le Roux and Sciacovelli (2019); however, the solar receiver part of the code was changed to include the cooling window.

It was assumed that the heat losses in the pipes connecting each of the components were negligible. To find the temperatures and pressures in the cycle, an iteration routine was used along with the recuperator effectiveness and the compressor and turbine isentropic efficiencies. Note that $P_1 = P_{10}$ (see Figure 1). By doing an exergy analysis for the recuperated solar-dish Brayton cycle and assuming $V_1 = V_{11}$ and $Z_1 = Z_{11}$, the net output power equation, Eq. (24) can be found (Le Roux, 2015). Eq. (25) shows the total entropy generation rate as a function of the pressures and temperatures of the cycle (see Figure 1).

$$\dot{W}_{net} = -T_\infty \dot{S}_{gen,int} + \left(1 - \frac{T_\infty}{T^*}\right)\dot{Q}^* + \dot{m}c_{p0}(T_1 - T_{11}) - \dot{m}c_{p0}\ln\left(\frac{T_1}{T_{11}}\right) \tag{24}$$

$$\begin{aligned}
\dot{S}_{gen,int} = & \left[-\dot{m}c_{p0}\ln\left(\frac{T_1}{T_2}\right) + \dot{m}R ln\left(\frac{P_1}{P_2}\right)\right]_{compressor} \\
& + \left[\dot{m}c_{p0}\, ln\left[\frac{T_{10}T_4}{T_9T_3}\left(\frac{P_{10}P_4}{P_9P_3}\right)^{-\frac{R}{c_{p0}}}\right] + \frac{\dot{Q}_{loss,reg}}{T_\infty}\right]_{recuperator} \\
& + \left[-\frac{\dot{Q}^*_{rec}}{T^*} + \frac{\dot{Q}_{loss,cond,rec}}{T_\infty} + \dot{m}c_{p0}\, ln\left(\frac{T_6}{T_5}\right) - \dot{m}R\, ln\left(\frac{P_6}{P_5}\right)\right]_{receiver} \\
& + \left[-\dot{m}c_{p0}\, ln\left(\frac{T_7}{T_8}\right) + \dot{m}R\, ln\left(\frac{P_7}{P_8}\right)\right]_{turbine}
\end{aligned}$$

$$+\left[-\dot{m}c_{p0}\ln\left(\frac{T_2}{T_3}\right)+\dot{m}R\ln\left(\frac{P_2}{P_3}\right)+\frac{\dot{Q}_{loss,win}}{T_\infty}-\frac{\dot{Q}^*_{win}}{T^*}\right]_{window} \quad (25)$$

Note that Eq. (25) indicates that the radiation and convection heat losses from the receiver's inner wall were absorbed by the window and the terms cancelled out in the entropy generation rate equations with only the conduction heat loss from the receiver still being present. The solar-to-mechanical efficiency was calculated with Eq. (26), where $\dot{Q}^*_{tot}$ included the solar heat gain of the receiver and the window.

$$\eta_{sol}=\frac{\dot{W}_{net}}{\dot{Q}^*_{tot}} \quad (26)$$

2.3.3 Energy utilisation factor

Another important cycle performance metric to consider was the energy utilisation factor (*EUF*), which indicated the extent to which the cycle could convert the available solar power into usable power and heat (Le Roux, 2018). The *EUF* was calculated by using Eq. (27):

$$EUF=\frac{\left(\dot{W}_{net}+\eta_{reg}\dot{Q}_{max,T_{11-1}}\right)}{\dot{Q}^*_{tot}} \quad (27)$$

where the quantity $\dot{Q}_{maxT_{11-1}}$ is the maximum potential for heat generation relative to the environment:

$$\dot{Q}_{max,T_{11-1}}=\dot{m}c_{p0}(T_{11}-T_1) \quad (28)$$

The temperature of the environment, T_1, was taken to be 300 K and the cycle's exhaust temperature, T_{11}, was calculated with the numerical analysis described in this section. The constant pressure specific heat, c_{p0}, was calculated at the average temperature between T_1 and T_{11}.

3 Results

3.1 Maximum solar-to-mechanical efficiency

Figure 3 shows the maximum solar-to-mechanical efficiency of the complete cycle with the included air-cooled window for four different receiver phase-change temperatures for the *GT2052* turbocharger as a function of turbine pressure ratio, represented by an optimal recuperator geometry (channel length, width and height, as well as the number of parallel flow channels).

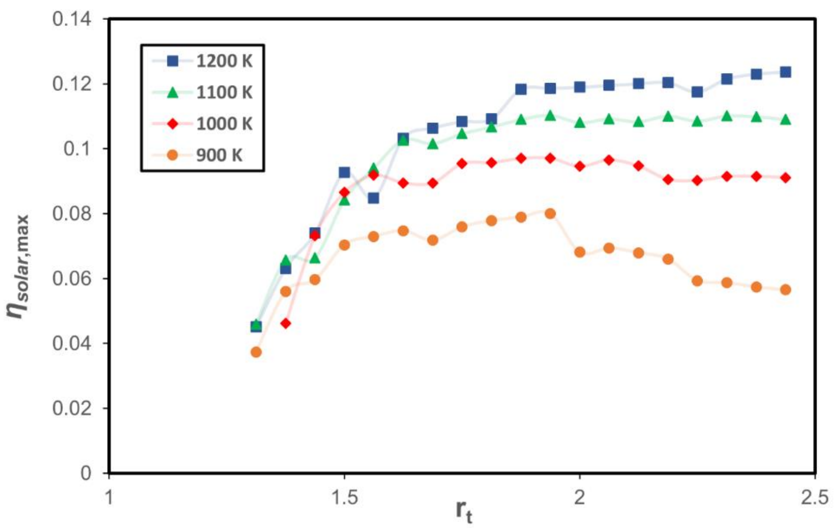

Figure 3. Maximum solar-to-mechanical efficiency of the cycle for different turbine pressure ratios and receiver phase-change temperatures from 900 K to 1200 K (for *GT2052*).

Figure 3 shows that the maximum solar-to-mechanical efficiency increased as the receiver surface temperature increased, especially at higher turbine pressure ratios. Figure 3 shows that maximum solar-to-mechanical efficiencies in the range of 4 % to 12 % could be achieved (at receiver temperatures of 900 K to 1200 K) with the *GT2052* turbocharger's range of pressure ratios. Figure 3 also shows that there were some outliers (or dips) in the solar-to-mechanical efficiency at certain pressure ratios, which is due to the code not solving within the specified number of iterations or tolerance. Table 2 shows the maximum data points correlating to Figure 3 for each receiver phase-change temperature and optimal recuperator geometry.

Table 2. Maximum solar-to-mechanical efficiency for *GT2052* and different surface temperatures.

T_s (K)	$r_{t,opt}$	a (mm)	b (mm)	L_{reg} (m)	n	$\dot{W}_{net}$ (W)	$Mass$ (kg)	$\dot{Q}^*_{tot}$ (kW)	$\eta_{sol,max,max}$
900	1.938	450	1.5	0.5	45	1985	325	24.8	0.080
1000	1.938	450	1.5	0.5	45	2703	325	27.8	0.097
1100	1.938	450	1.5	0.5	45	3454	325	31.3	0.110
1200	2.375	450	2.25	0.5	45	6098	326	49.6	0.123

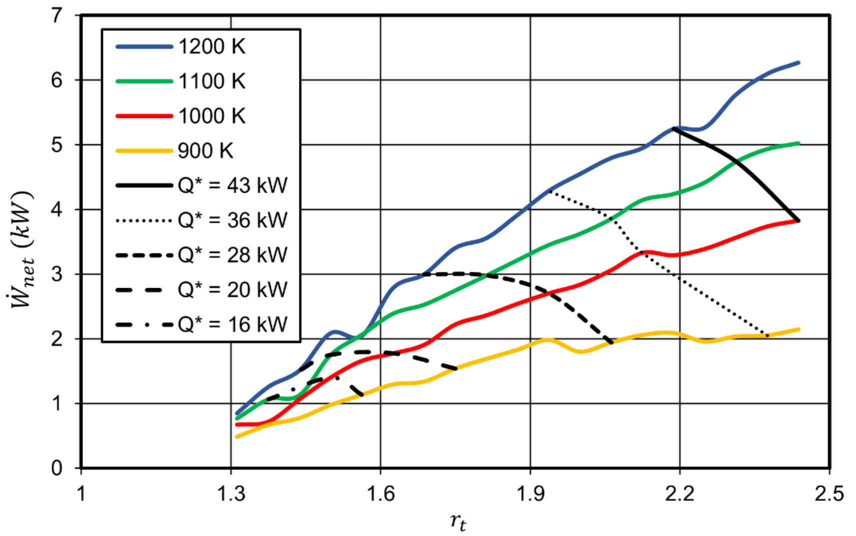

Figure 4. Net power output at maximum solar-to-mechanical efficiency as a function of turbine pressure ratio, receiver phase-change temperatures (900 K - 1200 K) and solar input power (for *GT2052*).

For the *GT2052* micro-turbine, Figure 4 indicates the cycle's net power output at the maximum solar-to-mechanical efficiency, depending on the turbine pressure ratio, together with the required solar power at the receiver aperture, $\dot{Q}^*$. The required solar power at the receiver aperture is an indication of the required dish size. Therefore, increased net power output could be produced by the cycle at higher pressure ratios and higher receiver phase-change temperatures. The required solar input power is also an indication of the cost of the solar dish because the aperture of the receiver was fixed at 0.25 m × 0.25 m (Le Roux & Sciacovelli, 2019). Therefore, an increased required solar input represents a larger solar dish and thus increased cost. Figure 4 can thus be viewed as a performance map because it can be used to select specific dish sizes to achieve a certain net power output at a preferred receiver phase-change temperature. As an example, Figure 4 indicates that for a solar dish with solar input power of $\dot{Q}^* = 28\,kW$, the expected shaft power output is 2 kW at a receiver phase-change temperature of 900 K and turbine pressure ratio of 2.06, while 3 kW shaft power can be produced at 1200 K and a much lower pressure ratio of 1.69 at the same required solar input power.

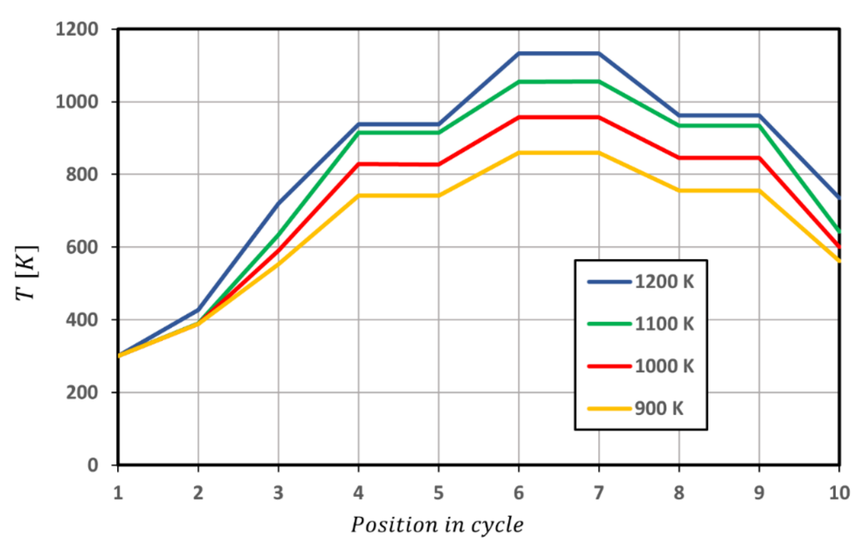

Figure 5. Temperature in the cycle at different receiver surface temperatures at maximum solar-to-mechanical efficiency (for *GT2052*).

Figure 5 shows the temperatures at the different positions throughout the cycle (see Figure 1 for the position numbering) for performance at maximum solar-to-mechanical efficiency when using a *GT2052* off-the-shelf turbocharger with the recuperator geometries mentioned in Table 2. Figure 5 shows that all of the temperature rise was for State 1 to State 6, which included the compressor, window, recuperator and the coiled tube. Figure 1 indicates that the window was between States 2 and 3, thus considering Figure 5, the window increased the air temperature on average by about 225 K. The window thus preheated the air before it entered the recuperator and receiver. Furthermore, the air leaving the cycle (at Position 10) was still at a relatively high temperature, which left much potential for cogeneration.

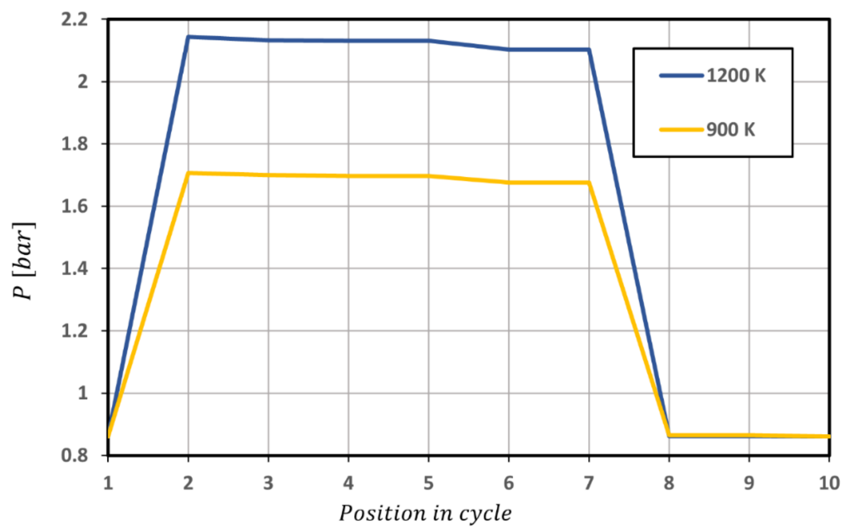

Figure 6. Pressure in the cycle at different receiver surface temperatures at maximum solar-to-mechanical efficiency (for *GT2052*).

Figure 6 shows the pressures at different positions in the cycle for different receiver phase-change temperatures for the *GT2052* micro-turbine operating at the maximum solar-to-mechanical efficiency and optimum pressure ratio (see Table 2). Since the turbochargers considered in this work were sensitive to pressure drop, the small pressure drop in the window (States 2 to 3) and the coiled tube (States 5 to 6) in Figure 6 was very important to allow for maximum inlet pressure at the turbine (State 7). The window accounted for between 0.7 kPa and 1.2 kPa of the total pressure drop in the cycle, which was considered acceptable in this study. It must be noted that for receiver phase-change temperatures 1000 K and 1100 K, the pressure in the cycle was the same as for the plotted receiver phase-change temperatures and is thus not shown in Figure 6.

3.2 Effect of the channel width

A parametric analysis was conducted with the *GT2052* micro-turbine at a fixed pressure ratio of 1.938 and recuperator dimensions of $a = 450$ mm, $b = 1.5$ mm, $L_{reg} = 0.5\ m$ and $n = 45$ channels (90 channels in total) (see Table 2). This allowed for easier comparison between the different receiver surface temperatures. The channel width was varied from 4.8 mm to 7.8 mm in 1 mm increments.

The pressure drop and temperature change of the air as it flowed through the cooling channel decreased as the channel width increased. Thus, a smaller channel width would cool the glass panes better than a larger channel width; however, a smaller channel width would lead to an increased pressure drop across the air-cooled window, which could be detrimental to the micro-turbine considered in this cycle. A trade-off would have to be made between having effective cooling of the glass and having a low enough pressure drop to ensure maximum inlet pressure at the turbine.

The solar-to-mechanical efficiency increased on average by about 1.3 % and the net power output by about 0.24 kW as the channel width increased from 4.8 mm to 7.8 mm. A larger channel width would thus be favourable when a large solar-to-mechanical efficiency and net power output were desired. The results also indicated that for a channel width of above 5.8 mm, the change in the solar-to-mechanical efficiency and net power output between the different channel widths becomes smaller relative to the previous channel width.

An average glass surface temperature over the two glass panes that form the cooling channel were calculated in the investigation. It was found that a smaller channel width had a lower average surface temperature per glass division and a lower receiver phase-change temperature also had a lower average glass surface temperature. As an example, if quartz glass was used for this application, which can be used at temperatures of 1300 K and above (Shelby & Lopes, 2005), a channel width of 7.8 mm and a receiver phase-change temperature of 1200 K would produce a maximum glass surface temperature of 1115 K, which might be too high for the glass to not shatter or crack.

A trade-off would have to be made between pressure drop and cooling effectiveness. Considering the above results, a channel width of 5.8 mm would produce a pressure drop of between 1 kPa and 1.2 kPa and a temperature change of the HTF over the window of between 170 K and 305 K for the different receiver surface temperatures. It would be worth investigating a cooling window channel width of between 5 mm and 5.8 mm at a receiver temperature of 900 K further to determine whether the glass would be safe to use continuously at high temperatures.

3.3 Performance impact of window

Table 3 summarises the optimum cycle properties with and without the proposed cooling window for each of the *GT2052* turbocharger. To compare the results of this study with the results of previous work by Le Roux and Sciacovelli (2019), in which the cycle had no window, the window code was simply added to the original code of Le Roux and Sciacovelli (2019) with the only modifications being that the recuperator length was allowed to range from 0.5 m to 3.5 m (instead of from 1.5 m to 4.5 m), and a lower tolerance of 0.01 for the iterations (higher resolution) was used. It should be noted that the properties given in Table 3 are for the optimum performance of the cycle (for maximum solar conversion efficiency).

Table 3. Comparison of cycle properties between the cycle with and without a cooling window for the *GT2052* turbo.

Turbo	T_s (K)		$r_{t,opt}$	a (mm)	b (mm)	L_{reg} (m)	n	$Mass$ (kg)	$\eta_{sol,max}$	$\dot{Q}^*_{tot}$ (kW)	$\dot{Q}_w$ (kW)	$\dot{W}_{net}$ (kW)	EUF
GT2052	900	Without window	1.938	450	1.5	0.5	45	325	0.152	13.0	5.5	2.0	58%
		With window	1.938	450	1.5	0.5	45	325	0.080	24.8	13.3	2.0	62%
	1000	Without window	1.938	450	1.5	0.5	45	325	0.182	14.6	5.4	2.7	55%
		With window	1.938	450	1.5	0.5	45	325	0.097	27.8	14.5	2.7	62%
	1100	Without window	1.938	450	1.5	0.5	45	325	0.201	16.6	5.3	3.3	52%
		With window	1.938	450	1.5	0.5	45	325	0.110	31.3	15.8	3.5	61%
	1200	Without window	2.375	450	1.5	0.5	45	325	0.220	26.5	8.9	5.8	56%
		With window	2.375	450	2.3	0.5	45	326	0.123	49.6	25.2	6.1	63%

Compared with the optimal recuperators in the cycles without the window, the optimal recuperators in the current study had the same dimensions for most of the results presented. The exceptions were at a receiver phase-change temperature of 1200 K, where the recuperator channel height was about 0.8 mm larger than for the cycle without the window.

For the *GT2052* turbocharger, a higher solar input power was required to reach maximum solar conversion efficiency than for the cycle without the window. Results also show that the maximum solar-to-mechanical efficiency was between 44 % and 47 % lower than for the cycle without a window. However, the *EUF* was between 7 % and 18 % higher than for the cycle without the cooling window. Note that a higher cycle exhaust temperature could lead to a higher *EUF* according to Eq. (27). The cycle exhaust temperature was between 38 % and 61 % higher for the *GT2052* turbocharger. A higher *EUF* means that the cycle converted the available solar power more efficiently into usable power and heat. The window essentially also acted as a heat exchanger that preheated the air before it went into the recuperator.

4 Conclusions and recommendations

This research considered an off-the-shelf turbocharger and different recuperator dimensions to determine the impact of a novel cooling window on the performance of a recuperated solar-dish Brayton cycle with a fixed solar receiver geometry operating at different PCM temperatures. The receiver considered in this study differed from those available in literature because a novel cooling window, using air directly from the compressor, was implemented on the inside of the receiver to reduce heat losses from the receiver to the environment. The results of the cycle utilising this receiver and novel cooling window were compared with the results of a previous study by Le Roux and Sciacovelli (2019), which did not include the cooling window.

Results showed that the required solar input power and the cycle's exhaust temperature were higher than for the cycle without the window. The maximum solar-to-mechanical efficiencies of the cycle with the novel cooling window were between 44 % and 47 % lower than for the cycle without a cooling window. However, the higher exhaust temperature of the cycle with the window led to a higher energy utilisation factor (*EUF*) than for the cycle without the window. The *EUF* was between 7 % and 18 % higher, and therefore, the cycle with the window had more potential for cogeneration, such as water heating or thermal energy storage. The cooling channel width had to be between 5 mm and 5.8 mm to keep the glass at a temperature of 1100 K or lower while maintaining an acceptable pressure drop across the cooling window.

This research served as an initial conceptual study from which further work could be done. There are a few possibilities regarding future work. The study only investigated the cooling channel width as a parameter and future work could include the cooling channel width as a variable in the study. The recuperator variables in this study were limited to a specific range (for the sake of comparison with previous work) and future work could include a larger range of variables to ensure a broader analysis of the cycle with the novel cooling window. A non-linear routine such as Newton's method could also be used to increase the accuracy of the glass surface temperature and net heat transfer rate calculations. Lastly, it is recommended that a cost analysis and optimisation be done to further compare the two cycles (with and without the cooling window). However, this conceptual study showed that it might not be feasible to implement the novel cooling window, except where a higher cycle exhaust temperature is preferred for cogeneration resulting in a higher *EUF*.

Nomenclature

A	Area	(m^2)
η	Efficiency	(-)
F	View factor	(-)
L	Length	(m)
$\dot{Q}$	Heat transfer rate	(W)
$\dot{Q}^*$	Rate of solar energy intercepted	(W)
$\dot{Q}$	Heat loss rate	(W)
$\dot{S}_{gen,int}$	Internal entropy generation rate	(W/K)
$\dot{W}$	Power	(W)

Subscripts

a	Air
abs	Absorbed
cav	Cavity
chn	Channel
cond	Conduction
conv	Convection
e	Exit
loss	Heat loss
n	Index counter
rad	Radiation
rec	Receiver
reg	Recuperator
s	Surface
sol	Solar
win	Window

References

Çengel, Y. A. & Ghajar, A. J. 2015. *Heat and Mass Transfer: Fundamentals and Applications,* 5th ed, New York, McGraw Hill Education.

Craig, K. J., Slootweg, M., Le Roux, W. G., Wolff, T. M. & Meyer, J. P. 2020. Using CFD and ray tracing to estimate the heat losses of a tubular cavity dish receiver for different inclination angles. *Solar Energy,* 211**,** 1137-1158.

Cui, F., He, Y., Cheng, Z. & Li, Y. 2013. Study on combined heat loss of a dish receiver with quartz glass cover. *Applied Energy,* 112**,** 690-696.

Fischer, S. & Hahne, E. 2000. The effect of different glass covers on the yearly energy gain of a solar collector. Stuttgart, Germany: University of Stuttgart.

Fuqiang, W., Jianyu, T., Lanxin, M. & Chengchao, W. 2014. Effects of glass cover on heat flux distribution for tube receiver with parabolic trough collector system. *Energy Conversion and Management,* 90**,** 47-52.

Gnielinski, V. 1976. New equations for heat and mass transfer in turbulent pipe and channel flow. *International Chemical Engineering,* 16**,** 359-368.

Le Roux, W. G. 2015. *Thermodynamic optimisation and experimental collector of a dish-mounted small-scale solar thermal Brayton cycle.* Thesis: University of Pretoria.

Le Roux, W. G. 2018. Feasibility study of a hybrid small-scale dish-mounted solar thermal Brayton cycle with cogeneration. Proceedings of the 16th International Heat Transfer Conference (IHTC16-24185), 2018 Beijing, China. 7929-7936.

Le Roux, W. G., Bello-Ochende, T. & Meyer, J. P. 2014. The efficiency of an open-cavity tubular solar receiver for a small-scale solar thermal Brayton cycle. *Energy Conversion and Management,* 84**,** 457-470.

Le Roux, W. G. & Sciacovelli, A. 2019. Recuperated solar-dish Brayton cycle using turbocharger and short-term thermal storage. *Solar Energy,* 194**,** 569-580.

McAdams, W. H. 1942. *Heat Transmission,* 2nd ed, New York, McGraw-Hill.

Paitoonsurikarn, S. & Lovegrove, K. 2003. On the study of convection loss from open cavity receivers in solar paraboloidal dish applications. Proceedings of the 40th ANZSES Conference, 26-29 November 2003 Melbourne, Australia.

Paitoonsurikarn, S. & Lovegrove, K. 2006. A new correlation for predicting the free convection loss from solar dish concentrating receivers. Proceedings of 44th ANZSES Conference, 13-15 September 2006 Canberra, Australia.

Paitoonsurikarn, S., Taumofeloau, T. & Lovegrove, K. 2004. Estimation of convection loss from paraboloidal dish cavity receivers. Proceedings of the 42nd ANZSES Conference, 28 November - 1 December 2004 Perth, Australia.

Pendyala, R., Wong, Y. S. & Ilyas, S. U. 2015. CDF Simulations of Natural Convection Heat Transfer in Enclosures with Varying Aspect Ratios. *Chemical Engineering Transactions,* 45**,** 793-799.

Petukhov, B. S. 1970. Heat Transfer and Friction in Turbulent Pipe Flow with Variable Physical Properties. *In:* HARTNETT, J. P. & IRVINE, T. F. (eds.) *Advances in Heat Transfer.* Elsevier.

Shelby, J. E. & Lopes, M. 2005. *Introduction to Glass Science and Technology,* Cambridge, United Kingdom, Royal Society of Chemistry.

Subedi, I., Silverman, T. J., Deceglie, M. G. & Podraza, N. J. 2019. Emissivity of solar cell cover glass calculated from infrared reflectance measurements. *Solar Energy Materials and Solar Cells,* 190**,** 98 - 102.

Wendelin, T., Dobos, A. & Lewandowski, A. 2013. SolTrace: a ray-tracing code for complex solar optical systems. National Renewable Energy Laboratory.